The Astrophysical Journal, 870:98 (15pp), 2019 January 10 https://doi.org/10.3847/1538-4357/aaf39e
© 2019. The American Astronomical Society. All rights reserved.

Black Hole Formation and Explosion from Rapidly Rotating Very Massive Stars

Haruki Uchida[1], Masaru Shibata[1,2], Koh Takahashi[3], and Takashi Yoshida[4]
[1] Center of Gravitational Physics, Yukawa Institute for Theoretical Physics, Kyoto University, Kyoto, 606-8502, Japan; haruki.uchida@yukawa.kyoto-u.ac.jp
[2] Max Planck Institute for Gravitational Physics (Albert Einstein Institute), Am Mühlenberg 1, Potsdam-Golm D-14476, Germany
[3] Argelander-Institut für Astronomie, Universität Bonn, D-53121 Bonn, Germany
[4] Department of Astronomy, Graduate School of Science, the University of Tokyo, Tokyo, 113-0033, Japan
Received 2018 September 23; revised 2018 November 12; accepted 2018 November 23; published 2019 January 14

Abstract

We explore the formation process of a black hole (BH) through the pair-instability collapse of a rotating Population III very massive star in axisymmetric numerical relativity. As the initial condition, we employ a progenitor star that is obtained by evolving a rapidly rotating zero-age main-sequence star with mass $320\,M_\odot$ until it reaches a pair-instability region. We find that for such a rapidly rotating model, a fraction of the mass, $\sim 10\,M_\odot$, forms a torus surrounding the remnant BH of mass $\sim 130\,M_\odot$, and an outflow is driven by a hydrodynamical effect. We also perform simulations, artificially reducing the initial angular velocity of the progenitor star, and find that only a small or no torus is formed and no outflow is driven. We discuss the possible evolution scenario of the remnant torus for the rapidly rotating model by considering the viscous and recombination effects and show that if an energy of $\sim 10^{52}$ erg is injected from the torus to the envelope, the luminosity and timescale of the explosion could be of the orders of 10^{43} erg s^{-1} and years, respectively. We also point out the possibility for observing gravitational waves associated with the BH formation for the rapidly rotating model by ground-based gravitational-wave detectors.

Key words: accretion, accretion disks – black hole physics – gravitational waves – hydrodynamics – stars: massive – supernovae: general

1. Introduction

Gravitational collapse induced by pair instability (PI) is one of the final fates of very massive stars (VMSs; Rakavy & Shaviv 1967; Rakavy et al. 1967; Barkat et al. 1967; Fraley 1968). In the carbon–oxygen (CO) core phase, if the CO core enters a region of low density ($\lesssim 10^6$ g cm^{-3}) and high temperature ($\gtrsim 10^9$ K), substantial electron–positron (e^+e^-) pair creation occurs, and then a pressure-averaged adiabatic index decreases below $4/3$. Then, the CO core becomes dynamically unstable and starts gravitational collapse. During the collapse, C and O in the CO core vigorously burn and release enormous rest-mass energy as thermal energy. If the injected thermal energy is sufficiently large, it may induce the disruption of the overall progenitor star (PI supernova [PISN]) or the ejection for an outer part of the star (pulsational-PISN; Woosley et al. 2007). If the injected thermal energy is not large enough to halt the collapse, these VMSs are expected to form black holes (BHs).

Under current theoretical understanding, a star with the mass of a CO core of $\gtrsim 130\,M_\odot$ collapses to a BH after the onset of the PI (Heger & Woosley 2002; Umeda & Nomoto 2002; Takahashi et al. 2016, 2018). This lower CO core mass limit is estimated to correspond to the zero-age main-sequence (ZAMS) mass $M_{\rm ZAMS} \gtrsim 260\,M_\odot$ for the case that there is no efficient (rotational) mixing with a sufficiently less efficient mass loss (Fryer et al. 2001; Heger & Woosley 2002). The lower ZAMS mass limit may be reduced if the effect of rotation is taken into account in the progenitor evolution because rotational mixing can recycle unprocessed material from the progenitor's outer envelope into the core, and thus, finally, the more massive CO core may be formed. In the case of rapidly rotating Population III stars, the ZAMS mass limit may reduce to $M_{\rm ZAMS} \gtrsim 190\,M_\odot$ (Chatzopoulos & Wheeler 2012; Yoon et al. 2012).

For metal-rich environments, the formation of a massive star that can form such a high-mass CO core is considered to be unlikely owing to efficient wind mass loss (Langer et al. 2007; Yoshida & Umeda 2011; Yusof et al. 2013; Yoshida et al. 2014). On the other hand, for metal-free environments, it has been speculated that such a massive star can be formed. A recent cosmological simulation indicates that ∼60% of first stars in number could have $M_{\rm ZAMS} > 240\,M_\odot$ (Hirano et al. 2015). There are two possible reasons for this high percentage. The first one is that the typical mass of the first stars can be as large as $\sim 100\,M_\odot$ owing to the lack of efficient coolants during its formation (e.g., Bromm & Larson 2004). The second one is that the rate of the line-driven wind mass loss is estimated to be too weak to reduce the total mass during the evolution (e.g., Krtička & Kubát 2009).

It is pointed out in the simulations of the first-star formation that rapidly rotating massive stars could be formed in a metal-poor environment (Greif et al. 2011; Stacy et al. 2013; Hirano et al. 2015). If a rotating VMS collapses to a BH, there is a possibility that some of the material of the star will form an accretion disk around the BH (Fryer et al. 2001; Shibata & Shapiro 2002). In our previous study for the gravitational collapse of rotating supermassive stars (SMSs) with mass $\gtrsim 10^5\,M_\odot$ (Uchida et al. 2017), which is a candidate for seeds of supermassive BHs found in the center of many massive galaxies, we found that if an SMS core is sufficiently rapidly rotating, a surrounding torus with a mass of ∼6% of the initial rest mass is formed after the BH formation and a fraction of the torus material is ejected as an outflow by a hydrodynamical effect.

If a gravitational collapse of a rotating VMS proceeds in the same way as the SMS, there is a possibility that a torus surrounding a rotating BH is formed and an outflow arises, leading possibly to an observable electromagnetic emission. As a pioneering study, Fryer et al. (2001) performed 1D stellar evolution calculations and axisymmetric (2D) gravitational collapse simulations of rotating VMSs. For the 2D simulations,

they used a Newtonian smoothed particle hydrodynamics code. They indicated that for the case of the VMS with the initial mass of $M_{\rm ZAMS} = 300\,M_\odot$ and rotating rigidly with the rotation velocity of 20% of the *Kepler* rotation at its surface, an He core with mass $\sim 180\,M_\odot$ is formed and it collapses to a BH. Although they were not able to follow the BH formation in their code, they indicated that a torus would be formed after the BH formation and the mass of the torus and BH would become ~ 30 and $\sim 140\,M_\odot$, respectively.

For an extension of their study, we perform simulations for the gravitational collapse of rotating Population III VMSs in axisymmetric numerical relativity. We use a realistic equation of state that includes the contribution from the pressure of gas, radiation, and degenerate electrons including e^+e^- pairs. For the nuclear reactions, we use the formulation that includes the effect of C, Ne, O, and Si burnings and photodissociation reaction including $^4{\rm He} \rightarrow 2p + 2n$. We also include approximately the effect of neutrino emission. The purpose of this paper is to explore the process of gravitational collapse of a rotating VMS to a BH. In particular, we pay attention to the properties of the torus and the process of generating an outflow during the formation process of the BH and torus.

This paper is organized as follows. In Section 2, we describe the setup of our numerical simulation. In Section 3, we describe the overview of the collapse, showing our results of numerical relativity simulations, and describe the processes of the BH formation, torus formation, and generating outflows for models with various rotational velocities. In Section 4, we discuss the possible evolution scenario of the torus by considering the viscous and recombination effects and estimate the bolometric luminosity of the explosion under the assumption that the energy injection from the torus to the envelope of the progenitor star occurs. We also discuss the possibility for observing gravitational waves associated with the BH formation for the rapidly rotating model. Section 5 provides a summary.

2. Numerical Setup

2.1. Stellar Evolution Phase

The stellar evolution code described in Takahashi et al. (2016, 2018) is used to calculate the evolution of zero-metallicity stars. A total of 47 isotopes are considered in the nuclear reaction network, which is capable of following the main reactions during the hydrostatic evolution of a massive star until the formation of an Fe core.

Effects of stellar rotation are taken into account by the formulation described in Takahashi et al. (2016). In this formulation, we assume that the star has a shellular rotation profile. The rotation-induced mixing and angular momentum transport are calculated by using a diffusion approximation. For the calculation of the diffusion coefficient, we consider the hydrodynamical instabilities of the Eddington–Sweet circulation, the Goldreich–Schubert–Fricke instability, the Solberg-Høyrand instability, and the dynamical and secular shear instabilities (Pinsonneault et al. 1989; Heger et al. 2000). At this stage, we consider only the effect of these hydrodynamical instabilities on the transport of angular momentum and do not consider the effects of other additional mechanisms.

We use the same equations of state as used in Takahashi et al. (2016) for 1D stellar evolution calculations. Stellar evolution is calculated from the ZAMS stage until the central temperature, $T_{\rm c}$, reaches $\log_{10} T_{\rm c}\ [{\rm K}] \approx 9.2$, at which the star is unstable to gravitational collapse owing to the PI. At this stage, we map the resulting 1D stellar evolution models onto 2D grids of axisymmetric gravitational collapse simulations as the initial conditions. For mapping the density, temperature, and chemical composition, we use the interpolation method described in Chen et al. (2011), with which the total mass, the internal energy, and the total mass of each element are guaranteed to be unchanged before and after the mapping. For the velocity profiles, we use the linear interpolation. Other variables are calculated by using the equation of state.

2.2. Gravitational Collapse Phase

For solving Einstein's evolution equations, we use the same method as in Shibata et al. (2016a). We employ the original version of the BSSN (Baumgarte–Shapiro–Shibata–Nakamura) formalism with a puncture gauge (Shibata & Nakamura 1995; Baumgarte & Shapiro 1999; Baker et al. 2006; Campanelli et al. 2006). In the 3 + 1 formulation, the metric is defined by the form

$$ds^2 = -\alpha^2 c^2 dt^2 + \gamma_{ij}(dx^i + \beta^i c dt)(dx^j + \beta^j c dt), \qquad (1)$$

where c is the speed of light and α, β^i, and γ_{ij} are the lapse function, the shift vector, and the induced metric on 3D spatial hypersurfaces, respectively. We also define the extrinsic curvature by

$$K_{ij} \equiv -\gamma_i{}^\alpha \gamma_j{}^\beta \nabla_\alpha n_\beta, \qquad (2)$$

where n^μ is a timelike unit-normal vector orthogonal to 3D hypersurfaces. In our BSSN formalism, we evolve $\rho_{\rm g} \equiv e^{-2\phi}$, $\tilde{\gamma}_{ij} \equiv \rho_{\rm g}^2 \gamma_{ij}$, $\tilde{A}_{ij} \equiv \rho_{\rm g}^2 (K_{ij} - \gamma_{ij} K^k_{\ k}/3)$, $K^k_{\ k}$, and $F_i \equiv \delta^{jk}\partial_j \tilde{\gamma}_{ik}$, where $\phi \equiv \ln({\rm det}\gamma_{ij})/12$. In the puncture gauge, we evolve $\rho_{\rm g}$ instead of ϕ and employ the gauge condition for the lapse function as

$$\frac{\partial \alpha}{\partial t} = -2\alpha K. \qquad (3)$$

It is known that this dynamical slicing has a strong singularity avoidance property in the BH spacetime and enables us to perform a long-term evolution after the BH formation. We use the standard fourth-order finite-differencing scheme to solve the gravitational-field equations (see chap. 3 of Shibata 2016 for a review).

We perform axisymmetric numerical simulations in cylindrical coordinates (X, Z) using a cartoon method for imposing axial symmetry (Alcubierre et al. 2001; Shibata 2003). A previous work of numerical relativistic 3D simulations of rotating stellar core collapse indicated that nonaxisymmetric deformation during the collapse did not occur unless the progenitor star is extremely rapidly and differentially rotating ($T_{\rm rot}/|W| \gtrsim 0.01$; e.g., Shibata & Sekiguchi 2005). Here $T_{\rm rot}$ and W are the initial total rotational kinetic energy and gravitational potential energy, respectively. In our models, $T_{\rm rot}/|W| \lesssim 0.003$, and thus the assumption of axial symmetry is reasonable during the collapse. After the collapse, it is suggested that the formed torus would also deform nonaxisymmetrically owing to hydrodynamics instabilities, which would induce the large mass accretion (e.g., Papaloizou & Pringle 1984; Tohline & Hachisu 1990). We discuss the

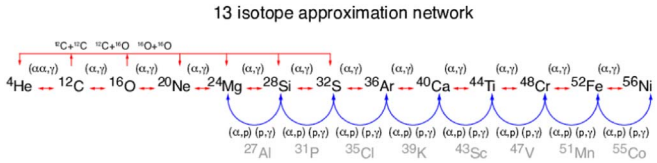

Figure 1. Isotopes included in the "approx13" nuclear reaction network code. This figure is taken from http://cococubed.asu.edu/code_pages/burn_helium.shtml.

possibility of the deformation of the torus due to the instabilities in Section 4.1.

A nonuniform grid is used for X and Z in the following manner. We define the grid spacing at the center by $\Delta X_0 \equiv X_1 - X_0$. Here $X_0 = 0$ and X_i is the location of the ith grid on which we assign all the physical variables. We set up the grid spacing for the inside and outside of $X_{\rm in}$ in the following manner: for $X_i < X_{\rm in}$, $\Delta X_i \equiv X_i - X_{i-1} = \Delta X_0$(const), and for $X_{\rm in} \leqslant X \leqslant X_{\rm max}$, $\Delta X_i = \eta \Delta X_{i-1}$, where η is a constant and $X_{\rm max}$ is the size of the computational domain along each axis. η determines the nonuniform degree of the grid spacing.

The grid parameters are set to be $(\Delta X_0, \eta, X_{\rm in}, X_{\rm max}) = (0.6R_M, 1.014, 18R_M, 3600R_M)$ until $\log_{10}T_{\rm c}\,[{\rm K}] = 10$, and then we perform a regrid changing the parameters as $(\Delta X_0, \eta, X_{\rm in}, X_{\rm max}) = (0.005R_M, 1.014, 0.4R_M, 2000R_M)$. Here $R_M \equiv GM/c^2$, where G and M are the gravitational constant and the total mass of the progenitor star at the end of the stellar evolution calculation, respectively. For the model of this paper, $M \approx 290\,M_\odot$ and $R_M \approx 4.3 \times 10^7$ cm (see Section 2.3). To confirm that numerical results with different grid resolutions agree reasonably with each other, we also perform a simulation with the low-resolution grid parameters such that $(\Delta X_0, \eta, X_{\rm in}, X_{\rm max}) = (0.007R_M, 1.014, 0.4R_M, 1700R_M)$ for the most rapidly rotating model (model a10; see Section 2.3). We show that the numerical results agree reasonably with each other for two resolution models in Section 3.3.

For 2D simulations, we use the Timmes & Swesty (2000) equation of state (EOS), which is approximately the same as that used in the 1D stellar evolution calculations. The EOS includes the contribution from radiation, ions as ideal gas, electrons, positrons, and corrections for Coulomb effects. For electrons and positrons, the relativistic effect, the effect of degeneration, and electron–positron pair creation are taken into account.

In order to include the energy generation by thermonuclear reactions and photodissociation reactions including $^4{\rm He} \rightarrow 2p + 2n$, the nuclear reaction calculation is divided into the following two categories. For $T < 5 \times 10^9$ K, we use the "approx13" nuclear reaction network code that includes the 13 α-chain elements (Timmes 1999). Figure 1 shows the 13 α-chain elements included in this code. On the other hand, for $T \geqslant 5 \times 10^9$ K, we assume that the abundances of isotopes are in a state of nuclear statistical equilibrium (NSE) and solve NSE equations including protons, neutrons, and 13 α-chain elements. In our calculation, we neglect the electron capture process, and thus we assume the electron fraction $Y_{\rm e} = 0.5$. We include the thermal effect of the nuclear reactions by using the same formulation as we described in Uchida et al. (2017).

In our calculation, the thermal neutrino energy loss is approximately included in the right-hand side of the equations of motion as

$$\nabla_\lambda T^{\lambda\mu} = \frac{u^\mu \rho}{c} q_{\rm neu}. \tag{4}$$

Here $T_{\mu\nu}$, u^μ, ρ, and $q_{\rm neu}$ are the energy momentum tensor, four-velocity, rest-mass density of fluid, and thermal neutrino emission rate, respectively. To calculate $q_{\rm neu}$, we use the analytic fitting formulae introduced in Itoh et al. (1996). Because neutrinos are optically thin for most regions of the collapsing star and remnant torus, we assume that neutrinos are entirely optically thin in this approximation. In reality, just before the BH formation, the matter density of the central region of the collapsing star exceeds 10^{11} g cm^{-3} and neutrinos would become optically thick. However, our simulations show that this region immediately falls into the BH. Hence, it would be safe to consider that the formulation of Equation (4) is applicable for our present study (see Section 3.1 for more details).

We confirmed that our 2D code successfully reproduces 1D results for a PISN calculation of a relatively low mass VMS (see the Appendix). This illustrates that with our prescription, the effect of key nuclear burning in the self-gravitating system is correctly taken into account.

2.3. Models

We select a progenitor ZAMS star with its initial mass $M_{\rm ZAMS} = 320\,M_\odot$. For the initial chemical composition, a result of the big bang nucleosynthesis (Steigman 2007) is used. For its initial rotation profile, we employed the rigid rotation with the rotation velocity of 50% of the *Kepler* rotation at its surface (the angular velocity and radius of the star are $\approx 2.1 \times 10^{-4}$ s^{-1} and $\approx 5.9 \times 10^{13}$ cm, respectively). As we already mentioned, we perform a stellar evolution calculation until $\log_{10}T_{\rm c}$ [K] reaches $\approx$9.2.

Figure 2 shows the profiles of the density and radius (top panel) and chemical distribution (bottom panel) of the progenitor star at the end of the stellar evolution calculation. The region of $\lesssim 150\,M_\odot$ is a compact core composed mainly of C and O, and the region of $\gtrsim 150\,M_\odot$ is a broadened envelope composed mainly of H and He. During the evolution, the star loses a part of its envelope owing to the mass loss, which is enhanced by the rotation (Langer 1998; Maeder & Meynet 2000). The total mass of the star at this end stage is $M \approx 290\,M_\odot$, and the outer edge of the CO core is located at a radius of $\approx 4.3 \times 10^{10}$ cm ($\approx 1000R_M$).

The angular velocity profile, ω, of this progenitor star is denoted by the black solid curve in Figure 3. The CO core approximately has a uniform rotation profile due to the convection that occurs in the entire He core during the He core burning phase. On the other hand, the envelope rotates approximately rigidly at a very small angular velocity of the order of 10^{-10} s^{-1}. This is due to the fact that during the late stage of the stellar evolution the convection occurs entirely in the envelope for this model, redistributing the angular momentum, and the rigid rotation state is achieved. Because of the expanded structure of the envelope (with the radius of its surface $\approx 3.6 \times 10^{14}$ cm), the angular velocity is much smaller than that of the core.

If additional angular momentum transport mechanisms were to work efficiently during the stellar evolution phase, the final core angular velocity would be reduced. For example, Takahashi et al. (2018) performed 1D stellar evolution

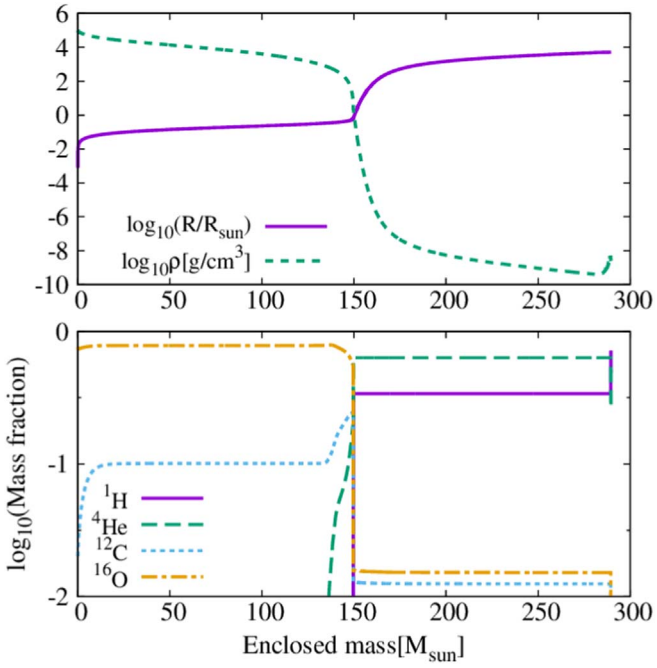

Figure 2. Progenitor profile of our model as functions of the enclosed mass at the end of the stellar evolution calculation. Top panel: radius (solid curve) and density (dashed curve) profiles. Bottom panel: chemical distribution. The solid, dashed, dotted, and dot-dashed curves show the chemical abundance of ^{1}H, ^{4}He, ^{12}C, and ^{16}O, respectively.

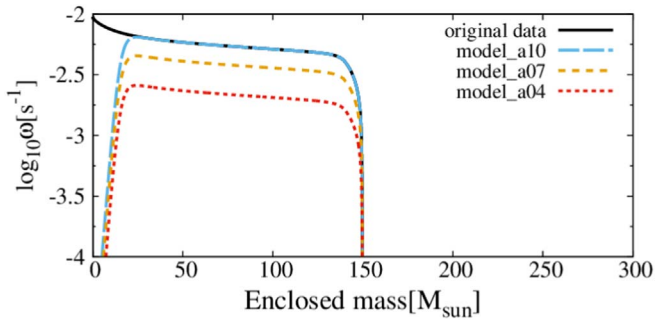

Figure 3. Angular velocity profile for the original data (solid curve) and models a10 (long-dashed curve), a07 (short-dashed curve), and a04 (dotted curve).

calculations of rotating VMSs with and without the effect of the magnetic stress modeled by the Tayler–Spruit dynamo (TS dynamo; Spruit 2002). They indicated that the magnetic models have 10 times slower rotation rate than the nonmagnetic models. To consider the case for which the angular velocity is decreased owing to such effects, we simulated two additional models for which the angular velocity is multiplied by a factor of 0.7 (model a07) and 0.4 (model a04), together with the original model (model a10).

At the start of simulations, we artificially reduce the angular velocity within a small central region of enclosed mass $\lesssim 30\,M_{\odot}$ for all the models. This is because the angular velocity profile for the original data sharply rises at the center, and hence the dimensionless spin parameter of the BH in the early stage of the collapse ($M_{\rm BH} \lesssim 30\,M_{\odot}$) becomes too large ($q_{\rm BH} \approx 1$), and numerical accuracy deteriorates at this time. Here $M_{\rm BH}$ and $q_{\rm BH}$ are the mass and dimensionless spin parameter of the BH, respectively. To avoid this difficulty, we initially reduce the angular velocity within the region of mass $\lesssim 30\,M_{\odot}$ for all the models. Since the total angular momentum of this inner region is only $\approx 1\%$ of the whole core, this handling would not affect strongly the properties of the final BH, torus, and outflow described in Section 3. The long-dashed, short-dashed, and dotted curves of Figure 3 show the angular velocity distribution for models a10, a07, and a04, respectively.

Before closing this section, we predict the mass and spin of the BH formed after the gravitational collapse of the core in these models. First, we calculate the quantities of the BH for the hypothetical case that the whole core collapses to form a BH. Then, the dimensionless spin parameter of the BH is estimated by $q_{\rm BH} \approx cJ_{\rm core}/GM_{\rm core}^2$, where $J_{\rm core}$ and $M_{\rm core}$ are the total angular momentum and mass of the core, respectively (for the original data, $J_{\rm core} \approx 2.2 \times 10^{53}\,{\rm g\,cm^2\,s^{-1}}$). Substituting $M_{\rm core} = 150\,M_{\odot}$, we find that $q_{\rm BH}$ for models a10, a07, and a04 are 1.1, 0.78, and 0.44, respectively. For model a10, $q_{\rm BH}$ exceeds 1. This suggests that all the fluid elements of the core would not collapse into a BH and that some elements are likely to form a torus around the BH for model a10.

Next, we analytically estimate $M_{\rm BH}$ and $q_{\rm BH}$ for all the models based on the method described in Shibata et al. (2016b). We describe briefly the method of the estimation. We assume that a seed BH is formed at the center of the collapsing VMS core and it dynamically grows while sequentially absorbing fluid elements from lower values of specific angular momentum, j. Then, we calculate approximately the mass, $m(j)$, and spin, $a(j) = cJ(j)/Gm(j)$, of the hypothetically growing BH at each moment by

$$m(j) = \int dV \rho \Theta(j - X^2\omega) \tag{5}$$

and

$$J(j) = \int dV \rho X^2 \omega \Theta(j - X^2\omega), \tag{6}$$

where $\Theta(x)$ is the step function, which satisfies $\Theta(x) = 1$ ($x \geqslant 0$) and $\Theta(x) = 0$ ($x < 0$). Here we neglect all the relativistic corrections in this analysis because they only give a minor contribution. Assuming that the BH is a Kerr BH, we can calculate $j_{\rm ISCO}(j)$ by inserting $m(j)$ and $a(j)$ into Equation (2.21) of Bardeen et al. (1972). Here $j_{\rm ISCO}$ is the specific angular momentum, which is needed for a test particle to rotate at an innermost stable circular orbit (ISCO) in the equatorial plane around the BH. We assume that the growth of the BH would terminate at the moment at which j becomes larger than $j_{\rm ISCO}(j)$. Then, we find that ($M_{\rm BH}$, $q_{\rm BH}$) for models a10, a07, and a04 are ($122\,M_{\odot}$, 0.83), ($147\,M_{\odot}$, 0.72), and ($150\,M_{\odot}$, 0.44), respectively. We expect that the remaining mass of the core will form a torus around the BH or be ejected as an outflow at the formation of a torus. For model a04, we find that all the fluid elements of the core are likely to form a BH.

3. Result

3.1. Before the BH Formation

First, we briefly describe the effect of nuclear reactions and neutrino emission until the BH formation. Although the time taken from the start of the gravitational collapse until the BH formation is different for each model owing to the difference of the centrifugal force strength, the qualitative feature of the

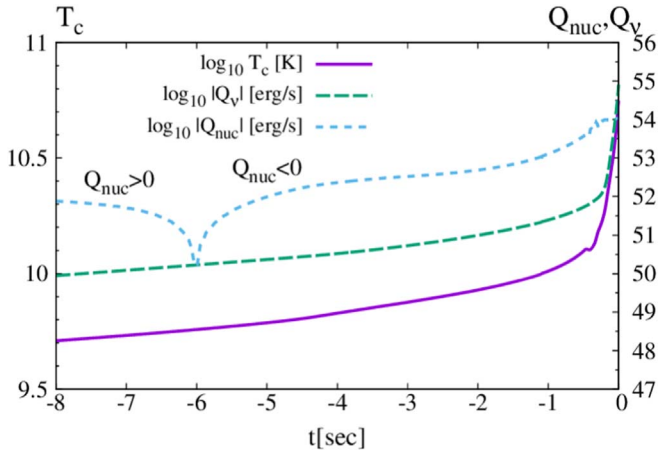

Figure 4. Time evolution of several quantities until the BH formation for model a10. The solid, dashed, and dotted curves show the central temperature, total neutrino emission rate, and total energy generation rate of the nuclear reactions, respectively. For $t \lesssim -6$ s, $Q_{\rm nuc} > 0$, and for $t \gtrsim -6$ s, $Q_{\rm nuc} < 0$. Here $t = 0$ is the time at which a BH is formed.

collapse dynamics depends weakly on the angular momentum for each model. Thus, we focus only on model a10. Hereafter, we take the time of the BH formation as the origin of time.

Figure 4 shows the time evolution of the central temperature (solid curve), total neutrino emission rate, Q_ν (dashed curve), and total energy generation rate of the nuclear reactions, $Q_{\rm nuc}$ (dotted curve), until the BH formation for model a10. Q_ν and $Q_{\rm nuc}$ are defined by

$$Q_\nu = \int \rho_* q_{\rm neu} \alpha d^3x \tag{7}$$

and

$$Q_{\rm nuc} = \int \rho_* q_{\rm nuc} \alpha d^3x, \tag{8}$$

respectively. Here $q_{\rm nuc}$ is the energy generation rate of the nuclear reactions and $\rho_* \equiv \rho u^t \sqrt{-g}$. Until $T_{\rm c} \lesssim 5 \times 10^9$ K ($t \lesssim -6$ s), the gravitational collapse is decelerated by the energy generation due to the nuclear burning. However, since our star model is massive enough, the collapse cannot be halted by the energy injection from the nuclear burning. Then, when $T_{\rm c}$ reaches $\sim 5 \times 10^9$ K ($t \gtrsim -6$ s), partial photodissociation reaction of heavy elements into ^{4}He occurs at the center, and thus the total energy generation rate of the nuclear reactions becomes a negative value. When $T_{\rm c}$ reaches $\sim 10^{10}$ K ($t \gtrsim -0.5$ s), photodissociation reaction of ^{4}He sets in at the center. Since this reaction increases the number density of nucleons, the gas pressure increases sharply at the center, and then the adiabatic index is slightly increased. However, this effect does not play a significant role for halting the collapse.

In our formulation, neutrinos take away a large amount of the thermal energy of the central region, and thus the central region collapses promptly to a BH. In reality, neutrinos in the high-density region with $\rho \gtrsim 10^{11}\,{\rm g\,cm^{-3}}$ would become optically thick, and thus the neutrino cooling would not be efficient in this region. In order to investigate this effect, we also performed a simulation for the same condition as model a10 but not including the neutrino emission (this corresponds to assuming that all neutrinos are trapped). We find that although the high-density core supported by the gas pressure is temporarily formed and the collapse is delayed by $\sim$0.3 s, the core immediately collapses to a BH and our final results do not change qualitatively.

3.2. After the BH Formation

Although the qualitative feature of the collapse dynamics until the BH formation depends weakly on it, the final outcomes depend strongly on the initial rotation velocity. In this section, we outline the process of the gravitational collapse after the BH formation for each model separately.

3.2.1. Model a10

Figure 5 displays the snapshots of the density profile after the BH formation for model a10. As already mentioned, the collapse cannot be halted by the energy injection from the nuclear burning, and thus a BH is formed at the center without any strong bounce (first panel of Figure 5). Indeed, the central density exceeds the nuclear density ($\sim 10^{14}\,{\rm g\,cm^{-3}}$) just before the BH formation ($t \gtrsim -5$ ms), and thus there is a possibility that a proto−neutron star (PNS) is formed temporarily at the center. However, this is not the case because the VMS that we consider here is massive enough. Nakazato et al. (2007) show that for the case of the gravitational collapse of mostly isentropic iron core with $s_{\rm i} > 7.5 k_{\rm B}$ (core mass $\gtrsim 10\,M_\odot$), the core collapses promptly to a BH without a quasi-stationary PNS formation. Here $s_{\rm i}$ and $k_{\rm B}$ are the initial specific entropy of the core and Boltzmann constant, respectively. Because the cores of our models are mostly isentropic and $s_{\rm i} \approx 15 k_{\rm B}$, it is safe to ignore the effect of the PNS formation for our models.

Since the fluid elements conserve their specific angular momentum, j, the growth of the BH is suppressed when their specific angular momentum is larger than $j_{\rm ISCO}$ for the growing BH. Here

$$j \equiv chu_\varphi, \tag{9}$$

where h and u_φ are the specific enthalpy and the azimuthal component of the four-velocity for the fluid, respectively. Fluid elements with $j > j_{\rm ISCO}$ form a torus surrounding the BH (second panel of Figure 5).

At the same time, a fraction of the fluid elements in the torus are pushed inward by the inertia of the entire torus matter, which has small infall velocity. Then, a part of material falling from a high latitude hits the inner part of the torus, and then, due to the strong encounter among the fluid elements, shocks are formed. As a result, a dense bubble (of a torus shape) is formed by the shock heating near the inner edge of the torus ($X \lesssim 5 \times 10^7$ cm; third panel of Figure 5).

Figure 6 displays the distribution of $j/j_{\rm ISCO}$ at $t = 1.20$ s. $j_{\rm ISCO}$ is calculated in the following manner. At $t = 1.20$ s, the mass and spin of the BH are $M_{\rm BH} \approx 112\,M_\odot$ and $a_{\rm BH} \approx 0.84 M_{\rm BH}$, respectively. Assuming that the BH is a Kerr BH, we calculate $j_{\rm ISCO}$ by inserting $M_{\rm BH}$ and $a_{\rm BH}$ into Equation (2.21) of Bardeen et al. (1972). Since a majority of the matter in this bubble has larger values of j than $j_{\rm ISCO}$ and is very hot, it does not accrete onto the BH and starts expanding as an outflow forming shocks (fourth and fifth panels of Figure 5).

The expansion of the shock front decelerates temporarily at (3–5) $\times 10^9$ cm away from the BH because the pressure behind the shock and the ram pressure of the infalling matter are balanced at this point (sixth panel of Figure 5). However, in a few seconds after the stalling of the shock, the expansion of the

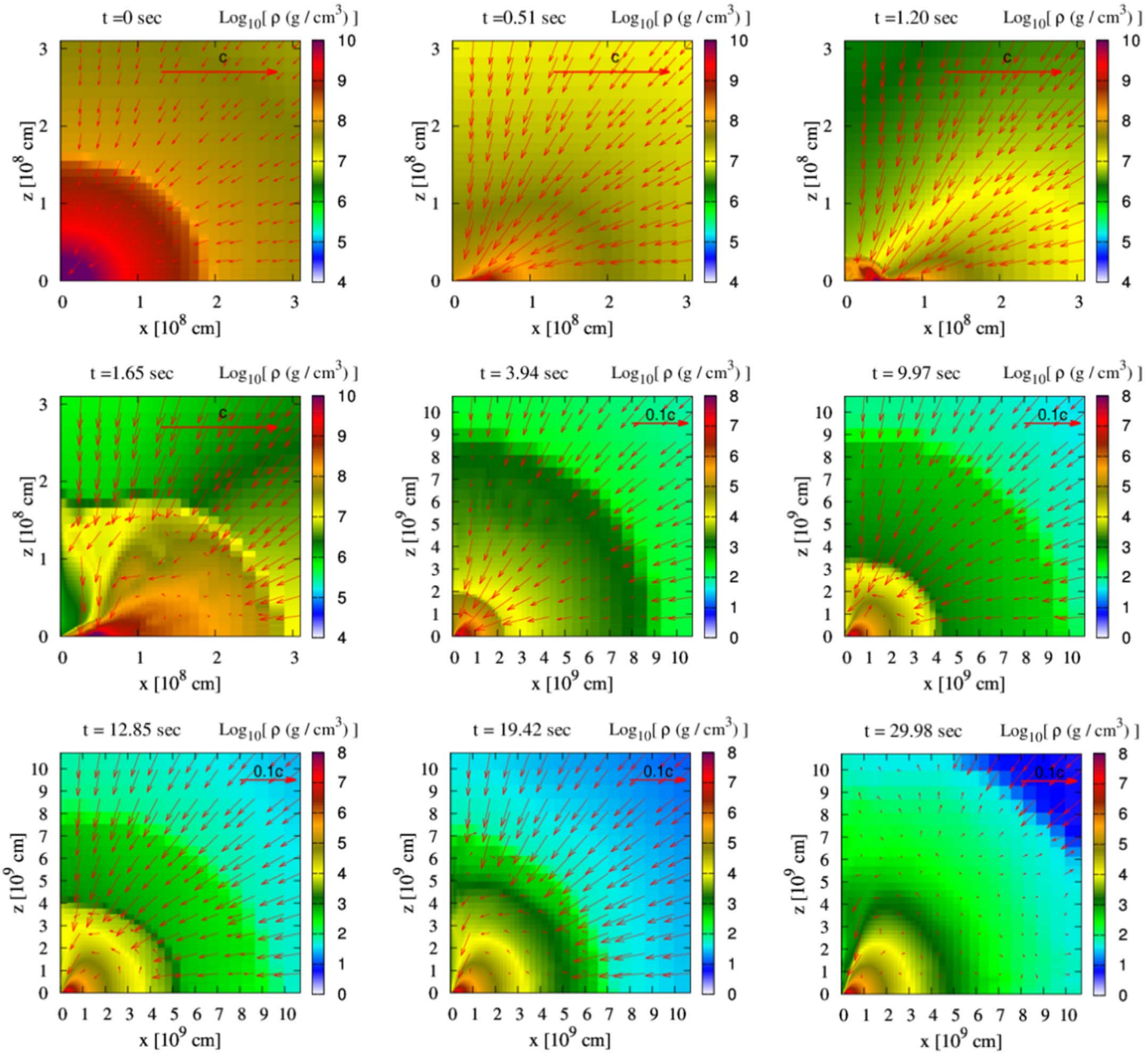

Figure 5. Snapshots of the density profiles during the VMS core collapse for model a10. The origin of time is taken at the time of the BH formation. The red arrows denote the velocity profile, $u^i/u^t(i = X, Z)$, which are normalized by c or $0.1c$, for which the size is indicated in the upper right corner of each snapshot. The fifth to ninth panels show zoom-out views of the outer region.

shock front sets in again because of the decrease of the density of the infalling matter and the resulting decrease of the ram pressure (seventh through ninth panels of Figure 5). At $t = 30$ s, the shock front is located at a radius of $\approx 10^{10}$ cm, and its expansion velocity is $\approx 5 \times 10^8\,\mathrm{cm\,s^{-1}}$. We estimate that the total energy of outflows (unbound fluid elements) injectable into the envelope is of the order of 10^{50} erg.

We define the total mass, $M_{>6}$, total internal energy, $E_{>6}$, and total neutrino emission rate, $Q_{\nu,>6}$, of the region with $\rho \geqslant 10^6\,\mathrm{g\,cm^{-3}}$. These quantities represent approximately the quantities of the torus. $M_{>6}$, $E_{>6}$, and $Q_{\nu,>6}$ are calculated by

$$M_{>6} = \int_{\rho \geqslant 10^6\ \mathrm{g\ cm^{-3}}} \rho_* d^3x, \tag{10}$$

$$E_{>6} = \int_{\rho \geqslant 10^6\ \mathrm{g\ cm^{-3}}} \rho_* \epsilon\ d^3x, \tag{11}$$

and

$$Q_{\nu,>6} = \int_{\rho \geqslant 10^6\ \mathrm{g\ cm^{-3}}} \rho_* |q_{\mathrm{neu}}| \alpha d^3x, \tag{12}$$

respectively. Here ϵ is the specific internal energy, and the integrations are performed outside the BH.

Figure 7 shows the time evolution of $M_{>6}$ (solid curve), $E_{>6}$ (dotted curve), and $Q_{\nu,>6}$ (dashed curve) for model a10. The bubble starts expanding and collides with the torus at $t \approx 1$ s. Then, the torus is heated up by the shock. For $t \gtrsim 4$ s, the shock front passes through the torus. Thereafter, the torus is gradually cooled by the neutrino emission. The mass of the torus is $\sim 12\,M_\odot$

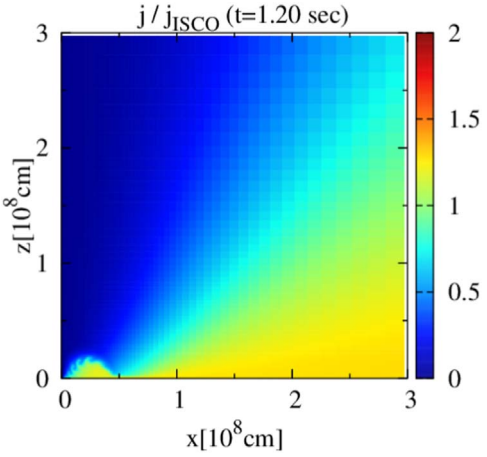

Figure 6. Distribution of $j/j_{\rm ISCO}$ of the torus for model a10 at $t = 1.20$ s. Here j is the specific angular momentum of the fluid elements and $j_{\rm ISCO}$ is the specific angular momentum, which is needed for a test particle to rotate at an ISCO in the equatorial plane around the BH.

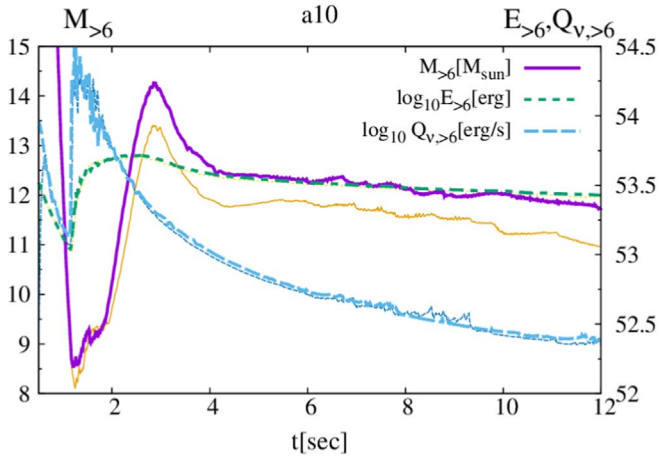

Figure 7. Time evolution of several quantities for model a10. The solid, dotted, and dashed curves show the total mass, internal energy, and neutrino emission rate of the region with $\rho \geqslant 10^6$ g cm^{-3}, respectively. The thin solid, thin dotted, and thin dashed curves show these quantities for the low-resolution case, respectively.

(approximately 8% of the initial rest mass of the CO core), and the neutrino cooling timescale $\tau_\nu \equiv E_{>6}/Q_{\nu,>6} \approx 10$ s at $t = 10$ s. At the end of the simulation, the torus relaxes to a quasi-stationary state.

Figure 8 displays the distributions of the density (left), temperature (middle), and mean nucleon number (right) of the torus for model a10 at $t = 10$ s. The maximum density and temperature of the torus are 6.7×10^9 g cm^{-3} and 2.1×10^{10} K, respectively. Due to such a high temperature, nearly the entire region of the torus is in a state of NSE. The distribution of the mean nucleon number shows that the torus is composed primarily of protons, neutrons, and ^{4}He generated by photodissociation. Total masses of nucleons (protons and neutrons) and ^{4}He in the torus at $t = 10$ s are $\sim$9.4 and 2.8 $M_\odot$, respectively.

3.2.2. Model a07

Figure 9 displays the snapshots of the density profile for model a07. For model a07, although the torus and outflow are formed in the same process as model a10, the shock front stagnates at a radius of $<10^9$ cm in several seconds after the BH formation and then falls by the ram pressure of the infalling matter at $t \gtrsim 8$ s. Figure 10 illustrates that the pressure behind the shock is defeated by the ram pressure, and hence the shock front falls toward the BH.

Figure 11 shows that the torus evolves approximately in the same process as model a10 for $t < 8$ s. However, for $t > 8$ s, the shock front falls down and the torus material accretes onto the BH. As a result, a small torus with mass $\sim$0.1 $M_\odot$ is formed at $t = 10$ s for this model.

3.2.3. Model a04

As we illustrate in Figures 12 and 13, no outflow occurs and no torus is formed for model a04. This is due to the fact that the specific angular momentum of the fluid elements is too small to remain around the BH. This result is consistent with what we expected in Section 2.3.

In conclusion, for the case in which we consider only the effects of the hydrodynamical instabilities on the transport of angular momentum in the stellar evolution calculation for rapidly rotating VMSs, approximately 8% of the initial rest mass of the CO core remains as the torus surrounding the BH and strong expanding shocks are formed. However, if the additional mechanisms (e.g., TS dynamo) decrease the rotation velocity even by 30%, finally a torus with an appreciable amount of mass is not formed, and outflow does not occur or accretes immediately onto the BH even if it is driven at the formation of a torus.

3.3. Properties of the BH

We list the quantities of the apparent horizon for all the models at $t = 10$ s in Table 1. Here $M_{\rm BH}^{\rm e}$ and $q_{\rm BH}^{\rm e}$ are the BH variables estimated in Section 2.3. In the following, we regard the mass and spin of the apparent horizon as those of the BH because at $t = 10$ s the spacetime becomes approximately stationary and it is known that the apparent horizon and the BH horizon agree in the stationary spacetime. For models a10 and a07, the mass of the BH is larger than the value estimated in Section 2.3. This is likely due to the fact that each fluid element of the VMS core falls toward the BH with an elliptical orbit, and then some fluid elements fall into the BH even if their specific angular momentum is larger than $j_{\rm ISCO}$. The pressure and geometry of the torus may also affect the result.

For $q_{\rm BH}$, model a07 has a larger value than $q_{\rm BH}^{\rm e}$. It is natural because the fluid elements with large specific angular momentum, which we did not expect to fall into the BH, actually fall, and if the whole core collapses to form a BH, $q_{\rm BH}$ is estimated to become $\sim$0.78 ($>q_{\rm BH}^{\rm e}$) for model a07 (see Section 2.3). However, for model a10, $q_{\rm BH}$ is lower than $q_{\rm BH}^{\rm e}$. This is due to the neutrino emission from the torus as we describe in the following.

For model a10, a large amount of neutrinos are emitted from the torus at the time when the torus is heated up by the shock (see Figure 7). Since the torus material is rotating with a relativistic velocity ($0.3c$–$0.4c$), the neutrinos take away a part of the angular momentum of the torus owing to the relativistic beaming effect. Thus, the specific angular momentum of the fluid elements that accretes onto the BH decreases. On the other hand, for model a07, the neutrino emission is not as strong as for model a10 because the mass of the torus is much smaller

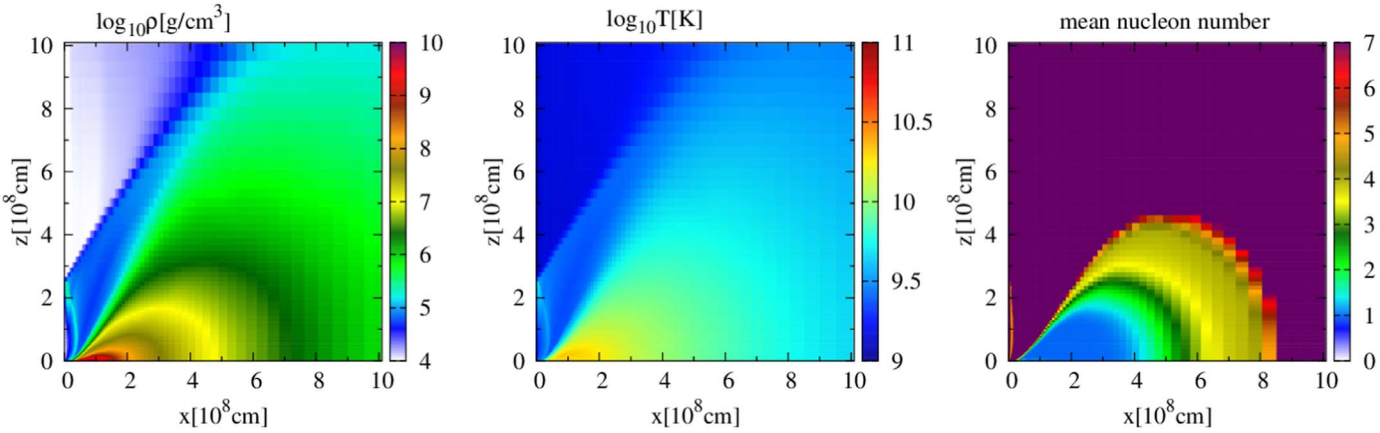

Figure 8. Rest-mass density (left), temperature (middle), and mean nucleon number (right) profiles of the torus for model a10 at $t = 10$ s.

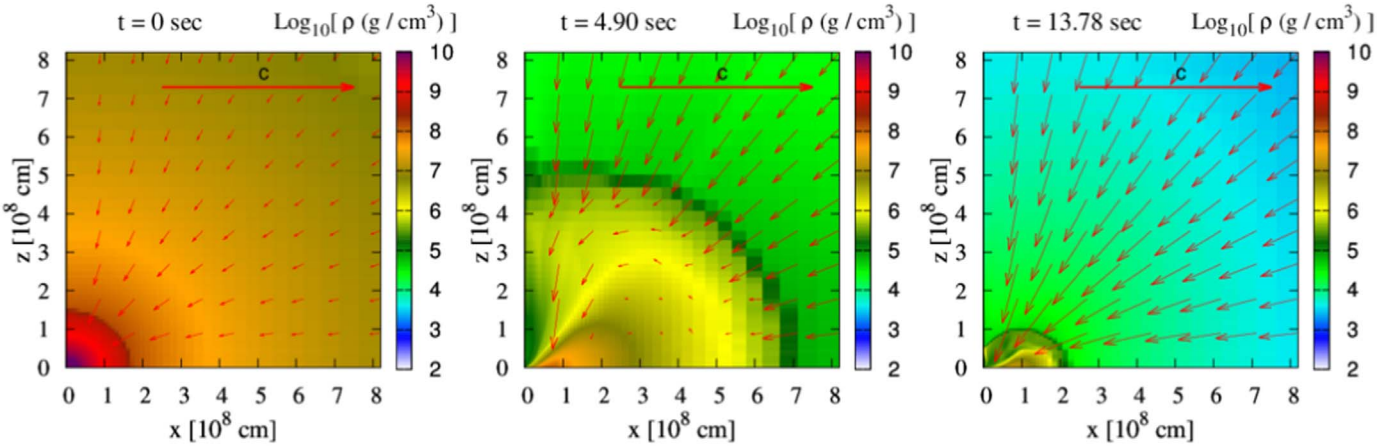

Figure 9. Same as Figure 5, but for model a07.

Table 1
The Key Parameters of the Apparent Horizon for All the Models at $t = 10$ s

Model	$M_{\rm BH}$	$q_{\rm BH}$	$M^{\rm e}_{\rm BH}$	$q^{\rm e}_{\rm BH}$
a10	131 $M_\odot$	0.79	122 $M_\odot$	0.83
a07	148 $M_\odot$	0.76	147 $M_\odot$	0.72
a04	148 $M_\odot$	0.44	150 $M_\odot$	0.44

Note. $M_{\rm BH}$ and $q_{\rm BH}$ are the mass and dimensionless spin parameter of the apparent horizon, respectively. Here $M^{\rm e}_{\rm BH}$ and $q^{\rm e}_{\rm BH}$ are the values estimated in Section 2.3.

than for model a10 (see Figure 11). Thus, the specific angular momentum of the fluid elements is not significantly taken away by neutrinos. For model a04, all the fluid elements of the core accrete to the BH with little neutrino emission, and thus the BH with an expected spin is formed.

3.4. Convergence

We note the convergence property of the numerical results. The thin solid, thin dotted, and thin dashed curves in Figure 7 show the time evolution of $M_{>6}$, $E_{>6}$, and $Q_{\nu,>6}$ for the low-resolution case for model a10, respectively. It is found that these quantities depend only weakly on the grid resolution. We check that the differences between the different resolution models at $t = 10$ s for $M_{>6}$, $E_{>6}$, and $Q_{\nu,>6}$ are within 6.0%, 4.3%, and 5.6%, respectively. We also check that the differences of $M_{\rm BH}$ and $q_{\rm BH}$ between the different resolution models at $t = 10$ s are within 0.4% and 1.3%, respectively. Thus, the agreement with different resolution models is reasonably achieved for these quantities.

4. Discussion

4.1. Evolution of the Torus

As we found in the previous section, after the gravitational collapse, a massive torus is formed around the BH and expanding shocks are launched for model a10. First, we briefly discuss the possible evolution scenario of the torus due to the viscous effect.

The last two panels of Figure 5 show that the infall velocity of the fluid elements inside the shock is much smaller than that on the outside. This suggests that the torus does not feel strong ram pressure of the infalling matter, and thus we expect that the evolution of the torus would be similar to that of an isolated torus.

We consider the possible viscous effect associated with magnetohydrodynamics (MHD) turbulence in the torus (e.g., Hawley et al. 2013; Suzuki & Inutsuka 2014; Salvesen et al. 2016; Shi et al. 2016), which is not taken into account in our present study, but it could play an important role for the evolution of the torus surrounding the BH in reality. We

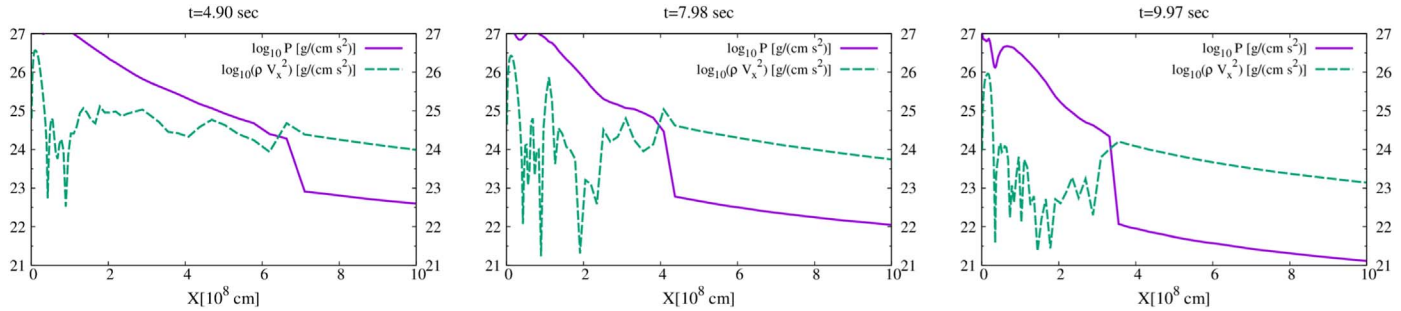

Figure 10. Snapshots of the pressure (solid curve) and ram pressure (ρV_X^2; dashed curve) profiles in the equatorial plane during the shock propagation for model a07. Here $V_X \equiv u^X/u^t$.

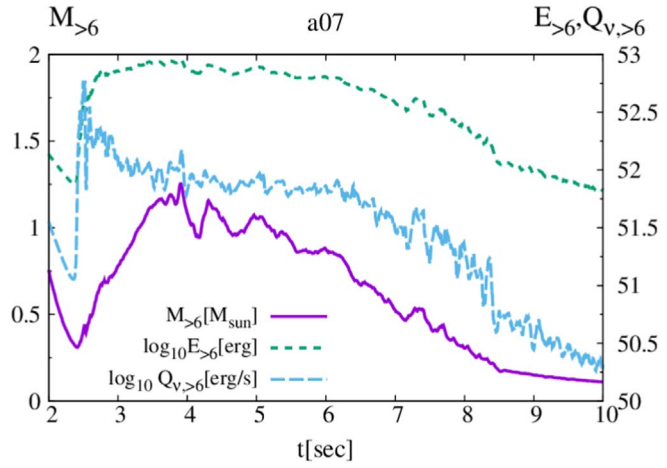

Figure 11. Time evolution of several quantities of the torus for model a07. The solid, dotted, and dashed curves show the total mass, internal energy, and neutrino emission rate of the region with $\rho \geqslant 10^6$ g cm^{-3}, respectively.

evaluate the strength of the viscosity by Shakura & Sunyaev's α-viscosity model (Shakura & Sunyaev 1973). In this model, the shear viscous coefficient can be written as

$$\nu = \alpha_{\rm vis} c_s H, \tag{13}$$

where $\alpha_{\rm vis}$ is the so-called α-viscosity parameter and c_s and H are the sound speed and the vertical scale height of the torus, respectively.

Assuming that the evolution of the torus could be described by a standard accretion disk theory (Shakura & Sunyaev 1973), the viscous timescale is estimated by

$$\begin{aligned} t_{\rm vis} &\sim \alpha_{\rm vis}^{-1}\left(\frac{R_{\rm torus}^3}{GM_{\rm BH}}\right)^{1/2}\left(\frac{H}{R_{\rm torus}}\right)^{-2} \\ &\approx 19\ {\rm s}\left(\frac{\alpha_{\rm vis}}{0.01}\right)^{-1}\left(\frac{M_{\rm BH}}{130M_\odot}\right)^{-1/2} \\ &\quad\times\left(\frac{R_{\rm torus}}{2\times10^8\ {\rm cm}}\right)^{3/2}\left(\frac{H/R_{\rm torus}}{1/3}\right)^{-2}, \end{aligned} \tag{14}$$

where $M_{\rm BH}$ and $R_{\rm torus}$ are the mass of the BH and the typical radial scale of the torus, respectively. Equation (14) shows that the viscous accretion timescale is of the order of 10 s for a plausible value of $\alpha_{\rm vis} = O(0.01)$ for model a10. Here $\alpha_{\rm vis} = O(0.01)$ is suggested to be a typical value for accretion disks by a number of high-resolution MHD simulations (Hawley et al. 2013; Suzuki & Inutsuka 2014; Salvesen et al. 2016; Shi et al. 2016).

The mass accretion could occur in this timescale, and matter in the outer part of the torus receives the angular momentum from its inner part. Then, the torus expands, and a part of its mass would be ejected. Fernández & Metzger (2013) and Just et al. (2015) showed that a fraction ($\sim$20%) of the matter of a torus surrounding a BH could be ejected by the viscous effect in the absence of strong cooling effects. Also, recent general relativistic MHD simulations showed that the total amount of the ejected mass could reach 20%–40% of the initial torus mass (Siegel & Metzger 2017; Fernández et al. 2019).

We expect that in the expanding torus and ejecta the recombination of light elements would occur and abundant thermal energy would be released (e.g., Fernández & Metzger 2013). The thermal energy released for the recombination of protons and neutrons to ^{4}He is

$$E_{2p+2n\rightarrow{}^4{\rm He}} \approx 1.4\times10^{52}\left(\frac{M_{p+n}}{M_\odot}\right){\rm erg}, \tag{15}$$

where M_{p+n} is the total mass of reacted protons and neutrons, which is assumed to be $\sim$10% of the torus mass.

Hence, if the nuclear reaction of protons and neutrons to ^{4}He occurs even with a few solar masses, explosive energy of the same order as the explosion energy of hypernovae ($\sim10^{52}$ erg) is released. If such an amount of thermal energy is efficiently deposited, the mass ejection would become stronger, and thus the ejecta would inject more energy into the envelope of the progenitor star. Then, the luminosity of the explosion would be high enough to be observed (see Section 4.2). Since we found that the cooling timescale by the neutrino emission of the torus is $\gtrsim$10 s, long-term simulations including both the neutrino cooling and viscous heating are necessary to follow the detailed time evolution of the torus. This is an interesting topic to be explored in the future.

We note that recent MHD simulations of the gravitational collapse of magnetized massive Population III stars and SMSs suggest that the magnetic field effects could launch a jet (Suwa et al. 2007; Sun et al. 2017, 2018). Such jets may also significantly inject the energy in the envelope.

Finally, we discuss the nonaxisymmetric instabilities of the torus. It is suggested that the torus would deform owing to the so-called Papaloizou–Pringle instability (Papaloizou & Pringle 1984). Previous general relativistic simulations show that the stability against the PPI depends on the profile of j and strength of the self-gravity of tori (Korobkin et al. 2011). If a torus is strongly self-gravitating and has the specific angular momentum distribution of the form of $j \propto X^\xi$, the torus is unstable to the PPI if $\xi \lesssim 0.25$ (Kiuchi et al. 2011). Figure 14 displays the density and specific angular momentum

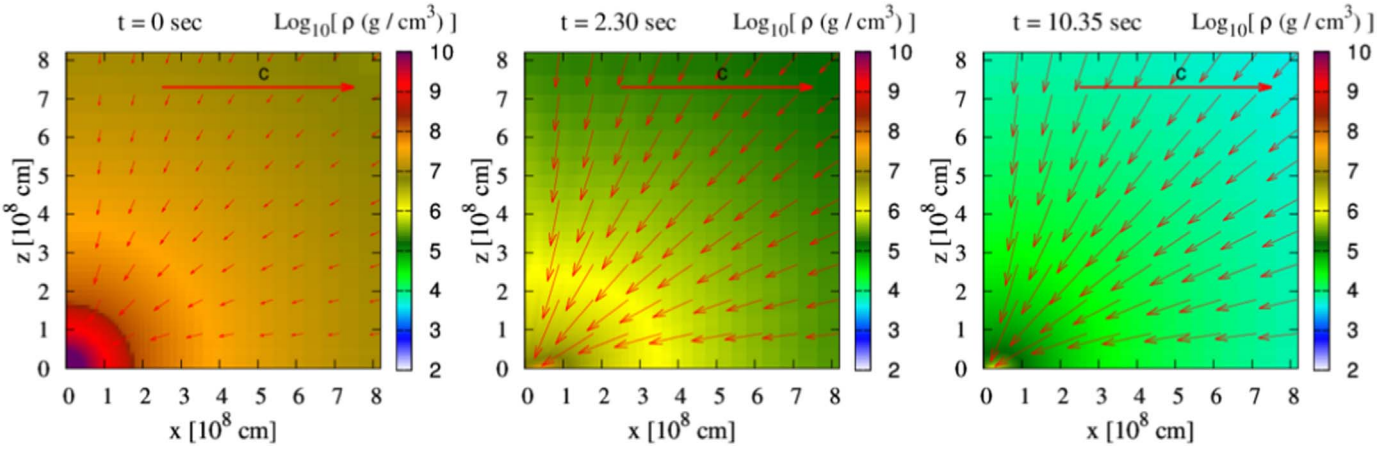

Figure 12. Same as Figure 9, but for model a04.

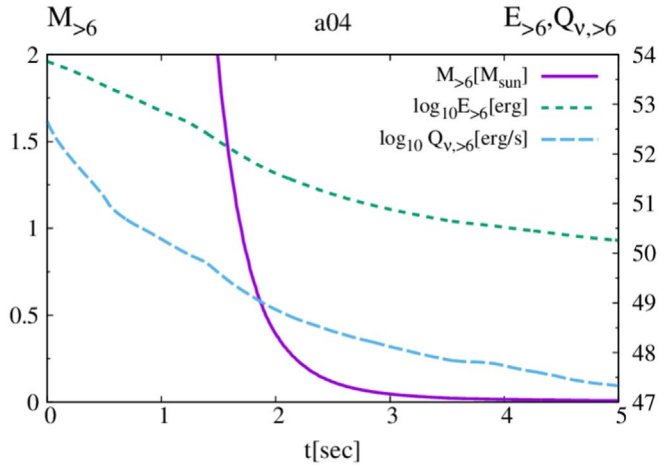

Figure 13. Same as Figure 11, but for model a04.

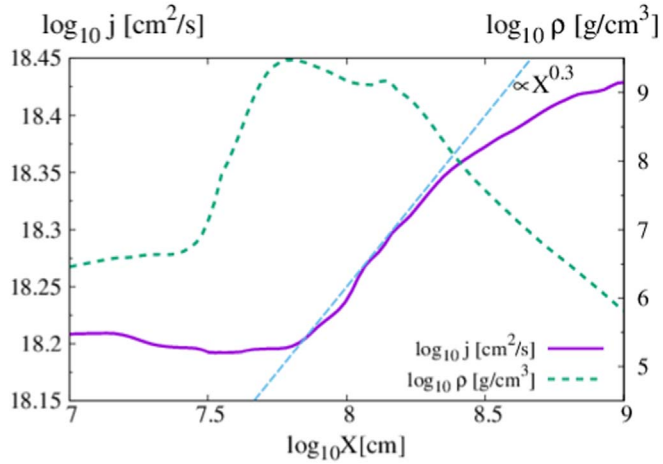

Figure 14. Profiles of the specific angular momentum (solid) and density (dotted) along the cylindrical coordinate on the equatorial plane for model a10 at $t \sim 30$ s. The dashed line denotes a slope proportional to $X^{0.3}$.

distribution of the torus along the cylindrical coordinate on the equatorial plane at $t \sim 30$ s. The torus found in our present study is also weakly self-gravitating and $\xi \approx 0$ at the density maximum, and hence it may be unstable. However, Bugli et al. (2018) showed that if the torus has a seed magnetic field, the MHD turbulence develops and the turbulent viscosity strongly suppresses the growth of the deformation. It is also suggested that if the self-gravitating torus has $T_{\rm tor}/|W_{\rm tor}| \gtrsim 0.16$, another nonaxisymmetric instability would arise where $T_{\rm tor}$ and $W_{\rm tor}$ are the total rotational kinetic energy and gravitational potential energy of the torus, respectively (e.g., Tohline & Hachisu 1990). We estimate $T_{\rm tor}/|W_{\rm tor}| \sim 0.2$ for model a10, and thus the torus may be unstable against the instability. Thus, to clarify whether the torus deforms nonaxisymmetrically, 3D MHD simulations will be needed for the future.

4.2. Explosion Luminosity

When the outflow and ejecta collide with the envelope, shocks are formed and propagate through the envelope. We have found in this study that the energy of the outflow is much less than the possible injection energy from the torus ejecta. Thus, in the following we take into account the energy injection only from the torus.

After the shock propagation, the matter in the envelope behind the shock is heated up, and when the shock reaches the surface of the envelope, it could be observed as an SN explosion. Since the expanding envelope is hydrogen-rich, this process is similar to the Type IIP SNe. Here we estimate the bolometric light curve of the hypothetical explosion by using the method of Arnett (1980) and Popov (1993) and following Appendix 4 of Nakauchi et al. (2013).

Arnett (1980) and Popov (1993) analytically formulated the light-curve model of the spherically expanding shock-heated ejecta. This formulation assumes that the explosion energy injected by the ejecta, $E_{\rm exp}$, is equally distributed into kinetic and internal energy, i.e., $E_{\rm exp}/2 = E_{\rm int} = E_{\rm kin}$, where $E_{\rm int}$ and $E_{\rm kin}$ are the total internal energy and kinetic energy of the envelope, respectively. The radius of the surface of the envelope, $R(t)$, is written as

$$R(t) \equiv R_0 + v_{\rm sc} t, \tag{16}$$

where R_0 is the initial radius of the envelope (for our model, $R_0 \approx 3.6 \times 10^{14}$ cm) and $v_{\rm sc}$ is the expansion velocity.

Assuming the uniform density profile and the homologous expansion, we have

$$\rho(t) = \frac{3M_{\rm env}}{4\pi R_0^3}\left(\frac{R(t)}{R_0}\right)^{-3}, \tag{17}$$

$$v(r, t) = \frac{r}{R(t)}v_{\rm sc}, \tag{18}$$

where r and $M_{\rm env}$ are the radial coordinate and total mass of the envelope, respectively. By using the equation of the kinetic energy, $E_{\rm kin} = \int_0^{R(t)} \rho v^2/2 \; dV$, $v_{\rm sc}$ is obtained as

$$v_{\rm sc} = \sqrt{\frac{10E_{\rm kin}}{3M_{\rm env}}} \approx 2.4 \times 10^8 \ {\rm cm\ s^{-1}} \times \left(\frac{E_{\rm exp}}{10^{52}\ {\rm erg}}\right)^{\frac{1}{2}}\left(\frac{M_{\rm env}}{150M_\odot}\right)^{-\frac{1}{2}}. \tag{19}$$

From the first law of thermodynamics, the thermal evolution of the envelope could be described by

$$\frac{\partial e}{\partial t} + P\frac{\partial}{\partial t}\left(\frac{1}{\rho}\right) = -\frac{\partial L}{\partial m_r}, \tag{20}$$

where e, P, L, and m_r are the specific internal energy, pressure, luminosity, and enclosed mass, respectively. We suppose that the envelope is radiation pressure dominant, i.e., $\rho e = 3P = aT^4$, where a is the radiation constant. In the diffusion approximation, L is written as

$$L = -\frac{4\pi r^2 ac}{3\kappa\rho}\frac{\partial T^4}{\partial r}. \tag{21}$$

Here κ is the opacity. For simplicity, we assume that κ is written as

$$\kappa = \begin{cases} \kappa_{\rm T} \approx 0.27\ {\rm cm^2\ g^{-1}} & (T \geqslant T_{\rm ion}), \\ 0 & (T < T_{\rm ion}), \end{cases} \tag{22}$$

where $\kappa_{\rm T}$ is the Thomson scattering opacity of the envelope (we assumed that the mass fractions of ^{1}H and ^{4}He of the envelope are $\sim$0.34 and $\sim$0.63, respectively) and $T_{\rm ion}$ is the hydrogen recombination temperature. We take $T_{\rm ion} = 6000$ K, and for the region $T < T_{\rm ion}$ we assume that the recombination of hydrogen atoms occurs and this region becomes optically transparent (Weaver & Woosley 1980; Litvinova & Nadezhin 1985).

We define the expansion time, $t_{\rm e}$, and the photon diffusion time, $t_{\rm d}$, as

$$t_{\rm e} \equiv \frac{R_0}{v_{\rm sc}} \approx 1.7 \times 10^6\ {\rm s} \times \left(\frac{R_0}{4 \times 10^{14}\ {\rm cm}}\right)\left(\frac{E_{\rm exp}}{10^{52}\ {\rm erg}}\right)^{-\frac{1}{2}}\left(\frac{M_{\rm env}}{150M_\odot}\right)^{\frac{1}{2}}, \tag{23}$$

$$t_{\rm d} \equiv \sqrt{\frac{9\kappa M_{\rm env}}{2\pi^3 v_{\rm sc} c}} \approx 4.0 \times 10^7\ {\rm s}\left(\frac{E_{\rm exp}}{10^{52}\ {\rm erg}}\right)^{-\frac{1}{4}}\left(\frac{M_{\rm env}}{150M_\odot}\right)^{\frac{3}{4}}. \tag{24}$$

Then, from Equations (20) and (22), the time evolution of the photosphere radius, $R_{\rm ph}(t)$, is obtained as

$$R_{\rm ph}(t) = \begin{cases} R(t) & (t \leqslant t_{\rm i}), \\ R_{\rm ion}(t) & (t > t_{\rm i}), \end{cases} \tag{25}$$

where

$$R_{\rm ion}(t)^2 = v_{\rm sc}^2\left\{\tau_{\rm i}\tau\left(1 + \frac{\tau_{\rm i}^2}{3t_{\rm d}^2}\right) - \frac{\tau^4}{3t_{\rm d}^2}\right\}. \tag{26}$$

Here $\tau \equiv t + t_{\rm e}$ and $\tau_{\rm i} \equiv t_{\rm i} + t_{\rm e}$. $t_{\rm i}$ is the time at which the surface effective temperature of the photosphere drops to $T_{\rm ion}$. The method for calculating $t_{\rm i}$ is described in the next paragraph.

The time evolution of the bolometric luminosity is obtained as

$$L(t) = \begin{cases} L_0 \exp\{-(t^2 + 2t_{\rm e}t)/t_{\rm d}^2\} & (t \leqslant t_{\rm i}), \\ 4\pi R_{\rm ion}(t)^2\sigma_{\rm SB}T_{\rm ion}^4 & (t > t_{\rm i}), \end{cases} \tag{27}$$

where

$$L_0 = \frac{t_{\rm e}E_{\rm exp}}{t_{\rm d}^2} \approx 1.0 \times 10^{43}\ {\rm erg\ s^{-1}} \times \left(\frac{R_0}{4 \times 10^{14}\ {\rm cm}}\right)\left(\frac{E_{\rm exp}}{10^{52}\ {\rm erg}}\right)\left(\frac{M_{\rm env}}{150M_\odot}\right)^{-1}. \tag{28}$$

Here $\sigma_{\rm SB}$ is the Stefan-Boltzmann constant. The effective temperature of the photosphere, $T_{\rm eff}$, can be given by the relation $L = 4\pi R_{\rm ph}^2\sigma_{\rm SB}T_{\rm eff}^4$, and $t_{\rm i}$ can be determined by solving the condition $T_{\rm eff}(t_{\rm i}) = T_{\rm ion}$. For the case of $t_{\rm i}^2 \ll t_{\rm d}^2$ and $t_{\rm e}t_{\rm i} \ll t_{\rm d}^2$, $t_{\rm i}$ is approximately given by

$$t_{\rm i} + t_{\rm e} \sim \left(\frac{L_0}{4\pi\sigma_{\rm SB}v_{\rm sc}^2}\right)^{\frac{1}{2}}T_{\rm ion}^{-2} \approx 1.4 \times 10^7\ {\rm s}\left(\frac{R_0}{4 \times 10^{14}\ {\rm cm}}\right)^{\frac{1}{2}}. \tag{29}$$

$R_{\rm ion}$ takes a maximum at $t = t_{\rm max}$, where

$$t_{\rm max} + t_{\rm e} \sim \left(\frac{3}{4}\right)^{1/3}\tau_{\rm i}^{1/3}t_{\rm d}^{2/3} \approx 2.5 \times 10^7\ {\rm s} \times \left(\frac{R_0}{4 \times 10^{14}\ {\rm cm}}\right)^{\frac{1}{6}}\left(\frac{E_{\rm exp}}{10^{52}\ {\rm erg}}\right)^{-\frac{1}{6}}\left(\frac{M_{\rm env}}{150M_\odot}\right)^{\frac{1}{2}}. \tag{30}$$

$R_{\rm ph}$ at $t = t_{\rm max}$ is given by

$$R_{\rm ph}(t_{\rm max}) \sim \left(\frac{3}{4}\right)^{2/3}v_{\rm sc}\tau_{\rm i}^{2/3}t_{\rm d}^{1/3} \approx 3.9 \times 10^{15}\ {\rm cm} \times \left(\frac{R_0}{4 \times 10^{14}\ {\rm cm}}\right)^{\frac{1}{3}}\left(\frac{E_{\rm exp}}{10^{52}\ {\rm erg}}\right)^{\frac{5}{12}}\left(\frac{M_{\rm env}}{150M_\odot}\right)^{-\frac{1}{4}}, \tag{31}$$

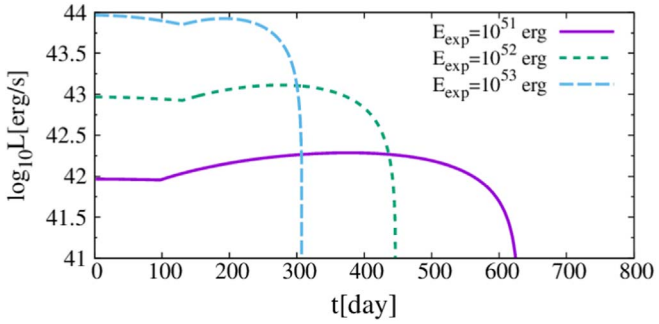

Figure 15. Time evolution of the bolometric luminosity described in Equation (27). We take $R_0 = 3.6 \times 10^{14}$ cm and $M_{\rm env} = 150\,M_\odot$. The solid, dotted, and dashed curves show the light curves for the case of $E_{\rm exp} = 10^{51}$, 10^{52}, and 10^{53} erg, respectively.

where we neglect the term $\tau_{\rm i}^2/3t_{\rm d}^2$ ($\ll$1). At this time, the bolometric luminosity also takes a maximum value,

$$L_{\rm max} \sim 4\pi R_{\rm ph}(t_{\rm max})^2\,\sigma_{\rm SB}\,T_{\rm ion}^4 \approx 1.4\times10^{43}\,{\rm erg\,s^{-1}} \times\left(\frac{R_0}{4\times10^{14}\,{\rm cm}}\right)^{\frac{2}{3}}\left(\frac{E_{\rm exp}}{10^{52}\,{\rm erg}}\right)^{\frac{5}{6}}\left(\frac{M_{\rm env}}{150M_\odot}\right)^{-\frac{1}{2}}. \quad (32)$$

Figure 15 shows the time evolution of the bolometric luminosity described in Equation (27). This shows that for the case of $E_{\rm exp} = 10^{52}$ erg, the bolometric luminosity becomes $\approx 10^{43}$ erg s^{-1} and its duration is of order 1 yr, which are similar to those of the peculiar hydrogen-rich SN (Arcavi et al. 2017).

4.3. Ring-down Gravitational Waves Associated with the Formation of BHs

Our previous studies for the gravitational collapse of rapidly rotating SMSs showed that burst gravitational waves are emitted in the formation process of rotating BHs and the total radiated energy, ΔE, is of the order of $10^{-6}M_{\rm BH}c^2$ (Shibata et al. 2016a; Uchida et al. 2017; see also Sun et al. 2017, 2018). Our preliminary simulations without the nuclear burning and neutrino emission show that during the BH formation in the collapse of rapidly rotating VMSs, gravitational waves are also emitted in a similar manner to those of SMSs.

Here we briefly estimate the frequency and amplitude of gravitational waves and discuss their observability for model a10. The frequency of gravitational waves, $f_{\rm gw}$, can be approximated by the frequency of the axisymmetric mode of the ring-down oscillation associated with the formed BH (Berti et al. 2009). Inserting $M_{\rm BH} = 131\,M_\odot$ and $a_{\rm BH} = 0.79M_{\rm BH}$ into Equation (97) of Berti et al. (2009), we obtain $f_{\rm gw} \approx 99$ Hz.

Following Shibata et al. (2016a), we suppose that the gravitational-wave amplitude would be approximately written as

$$h \sim \frac{4GM_{\rm BH}}{c^2D}\sqrt{\epsilon_{\rm gw}}, \approx 1.6\times10^{-22}\left(\frac{M_{\rm BH}}{131M_\odot}\right)\left(\frac{D}{100\,{\rm Mpc}}\right)^{-1}\left(\frac{\epsilon_{\rm gw}}{10^{-6}}\right)^{1/2}, \quad (33)$$

where D is the luminosity distance to the source and $\epsilon_{\rm gw} \equiv \Delta E/M_{\rm BH}c^2$. We take $D = 100$ Mpc, which is the same order as the luminosity distance of the peculiar hydrogen-rich SN (Arcavi et al. 2017). Thus, if $\epsilon_{\rm gw} = O(10^{-6})$ and the collapse of a VMS occurs at $D \sim 100$ Mpc, gravitational waves observed will be in the sensitive observation band of ground-based gravitational-wave detectors (e.g., Advanced LIGO; Abbott et al. 2017), in particular future ground-based detectors such as the Einstein telescope (Hild et al. 2011). It is our future work to investigate the observability of these gravitational waves in more detail.

4.4. Remarks

It is uncertain whether rapidly rotating VMSs in isolation could result in rapidly rotating CO cores such as those investigated in this work. On one hand, the slow rotation rates of neutron stars (Heger et al. 2000), white dwarfs (Suijs et al. 2008), and red giant cores (Mosser et al. 2012) suggest that the angular momentum transport in a star is more efficient than that expected from the hydrodynamical instabilities. On the other hand, progenitor stars of GRBs are considered to be massive stars that have a rapidly rotating core (Woosley 1993; MacFadyen & Woosley 1999). That is, even though there are efficient angular momentum transport mechanisms, special evolution paths that can form a rapidly rotating core should exist (e.g., binary merger, Fryer & Woosley 1998; Fryer & Heger 2005; chemically homogeneous evolution, Yoon & Langer 2005; Woosley & Heger 2006). Thus, VMSs with rapidly rotating CO cores are likely to be formed by such special evolution scenarios.

5. Conclusion

We explored the gravitational collapse of rotating VMSs in axisymmetric numerical relativity. We selected a progenitor ZAMS star with the initial mass of $M_{\rm ZAMS} = 320\,M_\odot$ and rotating rigidly with the rotation velocity of 50% of the *Kepler* rotation at its surface.

A 1D stellar evolution calculation is performed from the ZAMS stage until the central temperature reaches $\log_{10}T_{\rm c}$ [K] ≈ 9.2 including the effects of angular momentum transport induced by hydrodynamical instabilities. At this stage, we mapped the resulting 1D stellar evolution models onto 2D grids of axisymmetric gravitational collapse simulations as the initial conditions. In the stellar evolution stage, we neglect the effects of other additional angular momentum transport mechanisms.

The additional mechanisms may increase the efficiency of angular momentum transport and decrease the final core angular velocity (for example, it is suggested that the TS dynamo would decrease it approximately by one order of magnitude; Takahashi et al. 2018). To consider the cases for which the angular velocity is decreased owing to such effects, we simulated two additional models for which the angular velocity is multiplied by a factor of 0.7 (model a07) and 0.4 (model a04) in addition to the original model (model a10).

We found that for all the models, a BH is formed promptly after the gravitational collapse. For model a10, a fraction of the accreted matter forms a torus surrounding the remnant BH and drives an outflow. The outflow expands to form shocks in the core. In a few seconds after the BH formation, the torus relaxes to a quasi-stationary state with mass $\approx 12\,M_\odot$ composed of protons, neutrons, and ^{4}He generated by photodissociation. On the other hand, for models a07 and a04, finally only a small or

no torus is formed, and outflow does not occur or accretes immediately onto the BH even if it is driven at the formation of a torus. This is because the specific angular momentum of all the fluid elements is too small to form a large torus and strong outflow.

We analyzed the parameters of the remnant BH formed after the gravitational collapse. For models a10 and a07, the resulting mass of the BH is larger than the expectation based on a method in Shibata et al. (2016b). This is because in our expectation we regard each fluid element of the VMS core as a test particle and assume that it has a circular orbit around the hypothetically formed BH. However, in reality, each fluid element of the VMS core falls in an elliptical orbit to the central BH and feels the pressure force. Hence, a fraction of the additional fluid elements fall into the BH even though they have specific angular momentum larger than the value of the ISCO. For the spin of the BH, model a07 results in a larger value than the expectation. It is natural because the fluid elements with large specific angular momentum, which we do not expect to fall into the BH, actually fall. On the other hand, model a10 results in a lower spin than the expectation. This is due to the neutrino emission from the torus. Since the torus rotating with relativistic velocity ($0.3c$–$0.4c$) emits a large amount of neutrinos for model a10, a part of the angular momentum of the fluid elements accreting to the BH is taken away by the neutrinos owing to the relativistic beaming effect. Thus, the resulting spin of the BH for model a10 becomes a lower value. On the other hand, for model a07, since the effect of the neutrino emission is minor, the angular momentum of the fluid elements is not significantly taken away by neutrinos. For model a04, all the fluid elements of the core accrete to the BH with little neutrino emission, and hence a BH with expected mass and spin is formed.

We discussed a possible evolution process of the torus for model a10. Because a strong outflow is driven soon after the BH formation in this model, the torus does not feel strong ram pressure of the infalling matter, and thus the evolution of the torus would be similar to that of an isolated torus. Assuming the α-viscosity model and that the evolution of the torus could be described by a standard accretion disk theory, we found that the viscous accretion timescale is of the order of 10 s for a plausible value of $\alpha_{\rm vis} = O(0.01)$ for model a10. Because the neutrino cooling timescale is longer than the viscous timescale, the torus is likely to expand and a part of its mass is ejected in the viscous timescale. We expect that in the expanding torus and ejecta the recombination of light elements would occur and abundant thermal energy would be released. If the nuclear reaction of protons and neutrons to ^{4}He occurs in the ejecta even with a few solar masses, explosive energy of the same order as explosion energy of hypernovae ($\sim 10^{52}$ erg) is released. If such an amount of thermal energy is efficiently deposited, the mass ejection would become powerful, and thus the ejecta would inject significant energy into the envelope.

We estimated bolometric luminosity and the timescale supposing that the energy injection from the torus to the envelope occurs, and after the energy injection, the envelope would be heated up and start expanding like in an SN explosion. We found that if the ejecta injects energy of the order of 10^{52} erg, the bolometric luminosity and timescale are of the order of 10^{43} erg s^{-1} and 1 yr, respectively.

We discussed the possibility for observing gravitational waves associated with the BH formation. We estimate the frequency and amplitude of gravitational waves for model a10 and find that if the total radiated energy is $O(10^{-6})\, M_{\rm BH}c^2$ and the collapse of a VMS takes $\sim$100 Mpc, the frequency and amplitude are $\sim$100 Hz and $\sim 10^{-22}$, respectively. These values are in the sensitive observation band of ground-based gravitational-wave detectors, in particular, future ground-based detectors such as the Einstein telescope. Exploring the observability of these gravitational waves in more detail is our future work.

We are grateful to Yudai Suwa for a helpful discussion. Numerical computations were performed on the supercomputer XC50 at CfCA of NAOJ and XC40 at YITP of Kyoto University. This work was supported by Grant-in-Aid for Scientific Research (grant nos. 16H02183, 16K17706, 16H05341, and 15H00782) of Japanese MEXT/JSPS. K.T. was supported by the Japan Society for the Promotion of Science (JSPS) Overseas Research Fellowships.

Appendix
Numerical Test: PISN Simulation

For a test calculation of our 2D gravitational collapse code, we performed a PISN simulation of a nonrotating VMS with the initial mass of $M_{\rm ZAMS} = 200\, M_\odot$ and zero metallicity. For the initial rotation profile of the progenitor ZAMS star, we employed the rigid rotation with the rotation velocity of 30% of the *Kepler* rotation at its surface (angular velocity $\approx 1.7 \times 10^{-4}$ s^{-1}). Figure 16 shows the density, radius profile (left panel), and chemical distribution (right panel) of the progenitor star at the end of the stellar evolution calculation. The total mass of the star at this stage is $M \approx 190\, M_\odot$ ($R_M \approx 2.8 \times 10^7$ cm), and the outer edge of the CO core is located at $\approx 3.9 \times 10^{10}$ cm ($\approx 1400 R_M$).

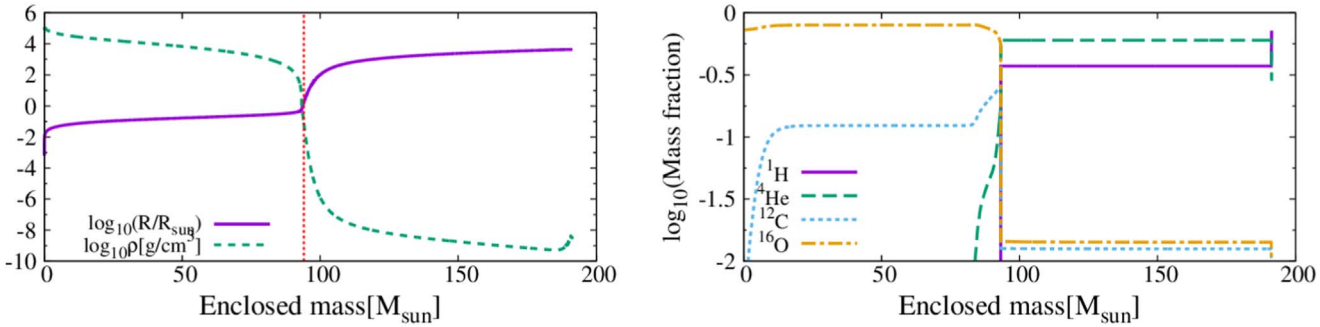

Figure 16. Progenitor profile of the model for the test calculation as functions of the enclosed mass at the end of the stellar evolution calculation. Left panel: density (solid curve) and radius (dashed curve) distribution. Right panel: chemical distribution. The solid, dashed, dotted, and dot-dashed curves show the chemical abundance of ^{1}H, ^{4}He, ^{12}C, and ^{16}O, respectively. The vertical red dotted line of the left panel denotes $X_{\rm max}$ of the test calculation.

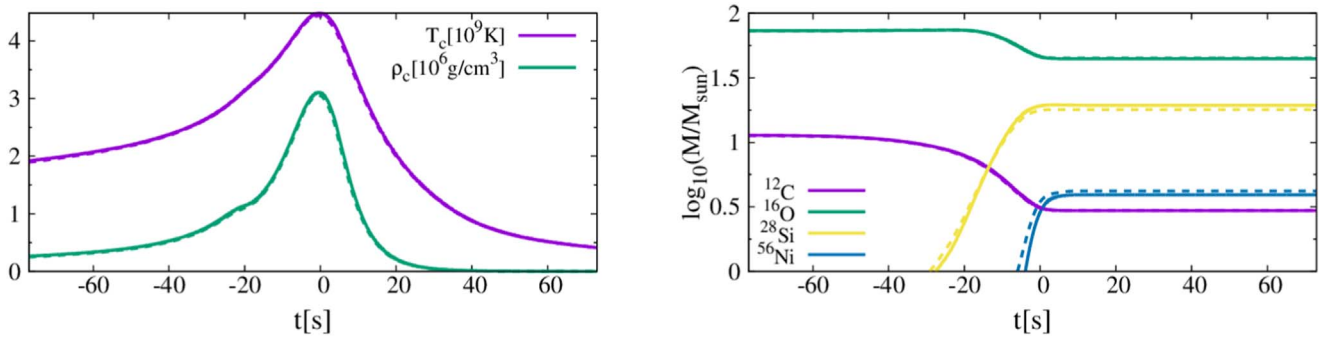

Figure 17. Time evolution of the central temperature and density (left panel) and total mass of each major element in the CO core (right panel). The origin of time is taken at the time at which the central density becomes the maximum value for each calculation. The solid and dashed curves show the results of 2D and 1D calculations, respectively.

We performed the 1D-spherical calculation in addition to the 2D calculation and compared the results of each calculation. For both 1D and 2D simulations, the rotational velocity is set to be zero initially. For the 1D calculation, the 1D-spherical general relativistic Lagrangian hydrodynamic code (Yamada 1997) with 47 isotopes in the reaction network are used. In this calculation, we use the same EOS as we used in the 1D stellar evolution calculations. For the 2D calculation, the grid parameters for the axisymmetric numerical simulation are set to be (ΔX_0, η, $X_{\rm in}$, $X_{\rm max}$) = ($2R_M$, 1.017, $40R_M$, $3400R_M$). The vertical red dotted line in the left panel of Figure 16 denotes $X_{\rm max}$. We added a perturbation that uniformly increases the internal energy by 1% at the start of calculation so that the maximum central temperature and density between the 1D and 2D calculations match.

Figure 17 shows the time evolution of central density and temperature (left panel) and total mass of each major element (right panel) in the CO core. The solid and dashed curves show the results of the 2D and 1D calculations, respectively. The origin of time is taken at the time at which the central density becomes the maximum value for each calculation. Figure 17 shows that the results of the 1D and 2D calculations are in good agreement. This indicates that our 2D code would be able to handle the gravitational collapse and explosion by the nuclear reaction as accurately as the 1D code.

ORCID iDs

Masaru Shibata https://orcid.org/0000-0002-4979-5671
Koh Takahashi https://orcid.org/0000-0002-6705-6303

References

Abbott, B. P., Abbott, R., Abbott, T. D., et al. 2017, CQGra, 34, 044001
Alcubierre, M., Brügmann, B., Holz, D., et al. 2001, IJMPD, 10, 273
Arcavi, I., Howell, D. A., Kasen, D., et al. 2017, Natur, 551, 210
Arnett, W. D. 1980, ApJ, 237, 541
Baker, J. G., Centrella, J., Choi, D.-I., Koppitz, M., & van Meter, J. 2006, PhRvL, 96, 111102
Bardeen, J. M., Press, W. H., & Teukolsky, S. A. 1972, ApJ, 178, 347
Barkat, Z., Rakavy, G., & Sack, N. 1967, PhRvL, 18, 379
Baumgarte, T. W., & Shapiro, S. L. 1999, PhRvD, 59, 024007
Berti, E., Cardoso, V., & Starinets, A. O. 2009, CQGra, 26, 163001
Bromm, V., & Larson, R. B. 2004, ARA&A, 42, 79
Bugli, M., Guilet, J., Müller, E., et al. 2018, MNRAS, 475, 108
Campanelli, M., Lousto, C. O., Marronetti, P., & Zlochower, Y. 2006, PhRvL, 96, 111101
Chatzopoulos, E., & Wheeler, J. C. 2012, ApJ, 748, 42
Chen, K.-J., Heger, A., & Almgren, A. S. 2011, CoPhC, 182, 254
Fernández, R., & Metzger, B. D. 2013, MNRAS, 435, 502
Fernández, R., Tchekhovskoy, A., Quataert, E., Foucart, F., & Kasen, D. 2019, MNRAS, 482, 3373
Fraley, G. S. 1968, Ap&SS, 2, 96
Fryer, C. L., & Heger, A. 2005, ApJ, 623, 302
Fryer, C. L., & Woosley, S. E. 1998, ApJL, 502, L9
Fryer, C. L., Woosley, S. E., & Heger, A. 2001, ApJ, 550, 372
Greif, T. H., Springel, V., White, S. D. M., et al. 2011, ApJ, 737, 75
Hawley, J. F., Richers, S. A., Guan, X., & Krolik, J. H. 2013, ApJ, 772, 102
Heger, A., Langer, N., & Woosley, S. E. 2000, ApJ, 528, 368
Heger, A., & Woosley, S. E. 2002, ApJ, 567, 532
Hild, S., Abernathy, M., Acernese, F., et al. 2011, CQGra, 28, 094013
Hirano, S., Hosokawa, T., Yoshida, N., Omukai, K., & Yorke, H. W. 2015, MNRAS, 448, 568
Itoh, N., Hayashi, H., Nishikawa, A., & Kohyama, Y. 1996, ApJS, 102, 411
Just, O., Bauswein, A., Ardevol Pulpillo, R., Goriely, S., & Janka, H.-T. 2015, MNRAS, 448, 541
Kiuchi, K., Shibata, M., Montero, P. J., & Font, J. A. 2011, PhRvL, 106, 251102
Korobkin, O., Abdikamalov, E. B., Schnetter, E., Stergioulas, N., & Zink, B. 2011, PhRvD, 83, 043007
Krtička, J., & Kubát, J. 2009, A&A, 493, 585
Langer, N. 1998, A&A, 329, 551
Langer, N., Norman, C. A., de Koter, A., et al. 2007, A&A, 475, L19
Litvinova, I. Y., & Nadezhin, D. K. 1985, SvAL, 11, 145
MacFadyen, A. I., & Woosley, S. E. 1999, ApJ, 524, 262
Maeder, A., & Meynet, G. 2000, A&A, 361, 159
Mosser, B., Goupil, M. J., Belkacem, K., et al. 2012, A&A, 548, A10
Nakauchi, D., Kashiyama, K., Suwa, Y., & Nakamura, T. 2013, ApJ, 778, 67
Nakazato, K., Sumiyoshi, K., & Yamada, S. 2007, ApJ, 666, 1140
Papaloizou, J. C. B., & Pringle, J. E. 1984, MNRAS, 208, 721
Pinsonneault, M. H., Kawaler, S. D., Sofia, S., & Demarque, P. 1989, ApJ, 338, 424
Popov, D. V. 1993, ApJ, 414, 712
Rakavy, G., & Shaviv, G. 1967, ApJ, 148, 803
Rakavy, G., Shaviv, G., & Zinamon, Z. 1967, ApJ, 150, 131
Salvesen, G., Simon, J. B., Armitage, P. J., & Begelman, M. C. 2016, MNRAS, 457, 857
Shakura, N. I., & Sunyaev, R. A. 1973, A&A, 24, 337
Shi, J.-M., Stone, J. M., & Huang, C. X. 2016, MNRAS, 456, 2273
Shibata, M. 2003, PhRvD, 67, 024033
Shibata, M. 2016, Numerical Relativity (Singapore: World Scientific)
Shibata, M., & Nakamura, T. 1995, PhRvD, 52, 5428
Shibata, M., Sekiguchi, Y., Uchida, H., & Umeda, H. 2016a, PhRvD, 94, 021501(R)
Shibata, M., & Sekiguchi, Y.-I. 2005, PhRvD, 71, 024014
Shibata, M., & Shapiro, S. L. 2002, ApJL, 572, L39
Shibata, M., Uchida, H., & Sekiguchi, Y. 2016b, ApJ, 818, 157
Siegel, D. M., & Metzger, B. D. 2017, PhRvL, 119, 231102
Spruit, H. C. 2002, A&A, 381, 923
Stacy, A., Greif, T. H., Klessen, R. S., Bromm, V., & Loeb, A. 2013, MNRAS, 431, 1470
Steigman, G. 2007, ARNPS, 57, 463
Suijs, M. P. L., Langer, N., Poelarends, A.-J., et al. 2008, A&A, 481, L87
Sun, L., Paschalidis, V., Ruiz, M., & Shapiro, S. L. 2017, PhRvD, 96, 043006

Sun, L., Ruiz, M., & Shapiro, S. L. 2018, PhRvD, 98, 103008
Suwa, Y., Takiwaki, T., Kotake, K., & Sato, K. 2007, PASJ, 59, 771
Suzuki, T. K., & Inutsuka, S.-i. 2014, ApJ, 784, 121
Takahashi, K., Yoshida, T., & Umeda, H. 2018, ApJ, 857, 111
Takahashi, K., Yoshida, T., Umeda, H., Sumiyoshi, K., & Yamada, S. 2016, MNRAS, 456, 1320
Timmes, F. X. 1999, ApJS, 124, 241
Timmes, F. X., & Swesty, F. D. 2000, ApJS, 126, 501
Tohline, J. E., & Hachisu, I. 1990, ApJ, 361, 394
Uchida, H., Shibata, M., Yoshida, T., Sekiguchi, Y., & Umeda, H. 2017, PhRvD, 96, 083016
Umeda, H., & Nomoto, K. 2002, ApJ, 565, 385
Weaver, T. A., & Woosley, S. E. 1980, in Ninth Texas Symp. on Relativistic Astrophysics 336, Annals of the New York Academy of Sciences, ed. J. Ehlers, J. J. Perry, & M. Walker (New York: New York Academy of Sciences), 335
Woosley, S. E. 1993, ApJ, 405, 273
Woosley, S. E., Blinnikov, S., & Heger, A. 2007, Natur, 450, 390
Woosley, S. E., & Heger, A. 2006, ApJ, 637, 914
Yamada, S. 1997, ApJ, 475, 720
Yoon, S.-C., Dierks, A., & Langer, N. 2012, A&A, 542, A113
Yoon, S.-C., & Langer, N. 2005, A&A, 435, 967
Yoshida, T., Okita, S., & Umeda, H. 2014, MNRAS, 438, 3119
Yoshida, T., & Umeda, H. 2011, MNRAS, 412, L78
Yusof, N., Hirschi, R., Meynet, G., et al. 2013, MNRAS, 433, 1114